

Article

# Impacts of 3D Aerosol, Cloud, and Water Vapor Variations on the Recent Brightening during the South Asian Monsoon Season

Zengxin Pan <sup>1</sup>, Feiyue Mao <sup>1,2,3,\*</sup>, Wei Wang <sup>1,4</sup> , Bo Zhu <sup>5</sup>, Xin Lu <sup>1</sup> and Wei Gong <sup>1,3,6</sup>

<sup>1</sup> State Key Laboratory of Information Engineering in Surveying, Mapping, and Remote Sensing, Wuhan University, Wuhan 430079, China; pzx@whu.edu.cn (Z.P.); wangweicn@whu.edu.cn (W.W.); xinlu@whu.edu.cn (X.L.); weigong@whu.edu.cn (W.G.)

<sup>2</sup> School of Remote Sensing and Information Engineering, Wuhan University, Wuhan 430079, China

<sup>3</sup> Collaborative Innovation Center for Geospatial Technology, Wuhan 430079, China

<sup>4</sup> School of Geoscience and Info-Physics, Central South University, Changsha 410083, China

<sup>5</sup> Hubei Provincial Environmental Monitoring Center Station, Wuhan 430072, China; zhubo125@whu.edu.cn

<sup>6</sup> Hubei Collaborative Innovation Center for High-efficiency Utilization of Solar Energy, Wuhan 430068, China

\* Correspondence: maofeiyue@whu.edu.cn

Received: 9 March 2018; Accepted: 20 April 2018; Published: 23 April 2018



**Abstract:** South Asia is experiencing a levelling-off trend in solar radiation and even a transition from dimming to brightening. Any change in incident solar radiation, which is the only significant energy source of the global ecosystem, profoundly affects our habitats. Here, we use multiple observations of the A-Train constellation to evaluate the impacts of three-dimensional (3D) aerosol, cloud, and water vapor variations on the changes in surface solar radiation during the monsoon season (June–September) in South Asia from 2006 to 2015. Results show that surface shortwave radiation (SSR) has possibly increased by  $16.2 \text{ W m}^{-2}$  during this period. However, an increase in aerosol loading is inconsistent with the SSR variations. Instead, clouds are generally reduced and thinned by approximately 8.8% and 280 m, respectively, with a decrease in both cloud water path (by  $34.7 \text{ g m}^{-2}$ ) and particle number concentration under cloudy conditions. Consequently, the shortwave cloud radiative effect decreases by approximately  $45.5 \text{ W m}^{-2}$  at the surface. Moreover, precipitable water in clear-sky conditions decreases by 2.8 mm (mainly below 2 km), and related solar brightening increases by  $2.5 \text{ W m}^{-2}$ . Overall, the decreases in 3D water vapor and clouds distinctly result in increased absorption of SSR and subsequent surface brightening.

**Keywords:** cloud; aerosol; water vapor; brightening; South Asia; A-Train

## 1. Introduction

Solar radiation incidence at the surface plays a fundamental and determinant role in the climate and life on our planet [1]. Surface solar radiation is a major component of the surface energy balance and governs many diverse surface processes, such as evaporation and associated hydrological components, plant photosynthesis, and the diurnal and seasonal courses of surface temperatures. Negative trends in the downwelling of surface solar radiation are collectively called “dimming”, whereas positive trends are called “brightening” [2]. Any change in the amount of solar radiation profoundly affects the temperature field, atmospheric and oceanic general circulation, and the hydrological cycle [3].

Widespread reduction in the annual average surface solar radiation, from the 1960s to the 1980s, has been reported by many researchers at the global and regional scales, including those from America, Europe, and China [2,4]. Subsequently, the term “brightening” was coined to emphasize the fact that

global solar radiation is no longer declining at many sites since the late 1980s [2]. Long, et al. [5] found that solar dimming has reversed at an increasing trend of  $6 \text{ W m}^{-2}$  per decade in the continental United States from 1995–2007. Wild [6] showed that the globally averaged trends in the 1980s typically reversed from dimming to brightening, while this study reports trends of  $2.2\text{--}6.6 \text{ W m}^{-2}$  per decade from the 1980s to the 2000s. However, developments in dimming and brightening after 2000 have shown mixed tendencies. Wild, et al. [7] reported a continuation of brightening at sites in Europe, United States, and parts of Asia, a levelling-off at sites in Japan and Antarctica, and indications of renewed dimming in China. Conversely, a recent and related study shows that brightening has continued in China since 2000 [8].

South Asia is endowed with abundant solar energy, given the geographic position of this region in the tropical belt [9]. Dimming or brightening is more evident and complicated in South Asia than in other regions, and its effects on regional and global climate and ecosystems are amplified by monsoon circulation (between June and September) in the region [1,10]. Although solar dimming had reversed after the late 1980s in other regions globally, Padma, et al. [10] found that the continued dimming of  $-8.6 \text{ W m}^{-2}$  per decade had occurred in India from 1981 to 2004 based on 12 stations over the Indian region. However, Wild, et al. [7] proposed to focus on the slight tendency towards the stabilizing of surface solar radiation that possibly began in the late 1990s. Furthermore, Soni, et al. [9] observed a trend reversal and partial recovery from dimming to brightening in India around 2001, but the related reasons are not determined.

Various mechanisms potentially contribute to dimming and brightening. Changes in surface solar radiation can be caused by either external changes in the amount of solar radiation incidents on the planet at the top of the atmosphere (TOA) or internal changes (within the climate system) in the transparency of the atmosphere, thereby modifying the solar beam on its way to the Earth surface. However, Willson and Mordvinov [11] verified that decadal dimming or brightening cannot be explained by changes in the luminosity of the sun because these changes are at least an order of magnitude smaller than those in climate systems. Therefore, the observed dimming or brightening must originate from alterations in the transparency of the atmosphere. Such alterations depend on the presence of clouds, aerosols, and radiatively active gases, particularly water vapor, which is a strong absorber of solar radiation [12].

Kvalevåg and Myhre [13] concluded that the major contributor to dimming, since pre-industrial times, is aerosols ( $-2.4 \text{ W m}^{-2}$ ) and that the secondary effect is the increase in gas concentrations ( $-0.64 \text{ W m}^{-2}$ ), including those of tropospheric ozone and water vapor. They also identified  $\text{NO}_2$ ,  $\text{CH}_4$ , and  $\text{CO}_2$  as minor contributors. Liepert [4] showed that the decrease in global radiation from 1961–1990 is attributable to the increases in cloud optical thickness and the direct effects of aerosols, thereby reducing solar radiation by 18 and  $8 \text{ W m}^{-2}$ , respectively. Kambezidis, et al. [14] argued that the decline in surface solar radiation in South Asia is attributable to the increase in the amount of anthropogenic aerosols from 1979 to 2004. This conclusion is supported by the agreement between the observed decadal changes in anthropogenic aerosol emissions and the trends in global solar radiation [6,15]. Solar dimming and brightening may be of a local or regional nature and are unavoidably influenced by regional sources and meteorology [9]. Here, we focus mainly on the dimming and brightening caused by changes in aerosols, water vapor, and clouds, which are the main factors that alter atmospheric transparency, and thus, regulate solar radiation incidences to the surface [6,9].

South Asia is experiencing a levelling-off trend in solar radiation and even a transition from dimming to brightening, but the related reasons are not determined. Therefore, this study used observations from multiple observations of the A-Train satellite constellation to evaluate the impacts of three-dimensional (3D) aerosol, cloud, and water vapor variations on the recent changes in surface solar radiation during the monsoon season (June–September) in South Asia from 2006 to 2015. The observations used mainly include CloudSat, Cloud-Aerosol Lidar and Infrared Pathfinder Satellite Observations (CALIPSO), Moderate Resolution Imaging Spectroradiometer (MODIS), and Clouds and the Earth's Radiant Energy System (CERES). Our study mainly aims to assess the connection between

variations in aerosols, clouds, and water vapor with respect to surface solar radiation, and identify the possible reasons for the recent brightening in South Asia.

## 2. Data and Methodology

### 2.1. Data Preparation

In this study, multiple sensors from A-Train are used to investigate the possible reasons for the dimming and brightening variations during the monsoon season (June–September) in South Asia from 2006 to 2015. The MYD08 and Level 2 aerosol layer products from MODIS and CALIPSO are used to describe the recent changes in aerosol loading in South Asia [16,17]. The CloudSat 2B-CLDCLASS, 2B-CWC-RO, and 2B-FLXHR products are used to quantify the 3D changes in cloud macrophysical and microphysical characteristics and corresponding variable radiative effects of clouds [18]. Moreover, environmental conditions are obtained from the European Centre for Medium-Range Weather Forecast-AUXiliary analysis (ECMWF-AUX) product [19]. The radiative transfer model of BUGSrad and ECMWF-AUX are used to evaluate the 3D changes in water vapor amount and related radiative forcing. The CERES/Aqua product is considered for evaluating the surface radiation energy variations [20]. The specific information about all sensors, products, and variables used in this study are collected and provided in Table S1. We define the study domain within South Asia to restrict the effect of surrounding land and sea pixels on the results of this study, as illustrated in Figure S1.

Moreover, aerosols detected by CALIPSO can be classified into the following six subtypes with high accuracy: clean marine, dust, polluted continental, clean continental, polluted dust, and smoke [21]. In this study, CALIPSO Level 2 aerosol layer products are used to describe the recent changes in aerosol loading and its mostly subtype component in South Asia. CALIPSO is highly sensitive to thin cirrus clouds but cannot easily penetrate optically thick layers with optical depths that exceed 3–5 [22,23]. In this case, CALIPSO determines a no or low aerosol optical depth (AOD) at near-surface due to the complete attenuation of lidar signals. To exclude the effects of unpenetrated profiles for lidar, we calculate the average AOD from CALIPSO only, based on the scene in which the lidar penetrates the entire atmosphere.

Furthermore, the 2B-FLXHR product is formed on the basis of the retrieved profiles of cloud macrophysical and microphysical properties from CloudSat, and is used to evaluate the radiative and heating rate forcing of 3D cloud variations. L'Ecuyer, et al. [18] detected biases between the radiative data of 2B-FLXHR from CloudSat and those from CERES with monthly 5° means on the global scale. The biases of outgoing shortwave (SW) radiation, outgoing longwave (LW) radiation, surface shortwave radiation (SSR), and surface LW radiation are less than 5.5 (6%), 0.1 (<0.1%), 16 (7%), and 13 W m<sup>-2</sup> (4%), respectively. Moreover, the uncertainties in 2B-FLXHR fluxes decrease significantly for long time scale averages [18]. Therefore, the radiative forcing of clouds, derived from CloudSat, have been verified as credible, especially in large space and time scales [18,24].

Strict selection procedures are implemented to control the quality of the data products, thereby ensuring credible conclusions. The cloud mask and radar reflectivity, from the CloudSat 2B-GEOPROF, are set to be more than 20 and −28 dBZ, respectively, and the quality flag from the 2B-CLDCLASS is identified as confidence to CloudSat [25]. We define the cloudy conditions for all products as the scenes in which the cloud mask from the CloudSat footprint exceeds 20, and the others are the clear-sky conditions. The probability of a false detection of clouds to CloudSat is less than 5% in comparison with that by CALIPSO under this cloud screening method [25]. Data quality for CALIPSO is maintained by screening the cloud layer with a high degree of confidence (>90%) [22]. We only use the radiative data from CERES with a sensor-viewing zenith angle less than 60° at the surface, to restrict the uncertainty from the satellite non-nadir point [20]. In this study, the SW solar radiation (<5 μm) that comprises more than 99.5% of total solar energy is assumed as the total incoming solar radiation at the TOA and surface. Although the BUGSrad defines the SW from 0–4 μm, the solar energy at 4–5 μm is excessively

low (approximately 0.39% of total solar energy) [18]. Therefore, the effect of this difference is ignorable in the definitions of the SW between CERES (0–5  $\mu\text{m}$ ) and BUGSrad (0–4  $\mu\text{m}$ ).

BUGSrad is the official radiative transfer model used by the product of CloudSat 2B-FLXHR [18,26]. This model is based on the two-stream doubling–adding solution to the radiative transfer equation with the assumption of a plane-parallel atmosphere [27]. BUGSrad computes molecular absorption and scattering properties based on correlated- $k$  formulation [26]. The model provides the two broadband-flux estimates. One broadband flux covers the SW at 0–4  $\mu\text{m}$ , and the other one covers the LW above 4  $\mu\text{m}$ . Based on the comparison experiment with observations of the Atmospheric Radiation Measurement program, the mean biases of SW and LW in clear-sky conditions are 1.2 and 2.2  $\text{W m}^{-2}$  at the TOA, respectively [27].

## 2.2. Methodology

We evaluated the total changes of aerosol, cloud, and water vapor, as well as their impacts on solar radiation during the monsoon season in South Asia. Therefore, we collocated all observations at a resolution of  $1^\circ \times 1^\circ$  and ignored the different resolutions of multiple sensors. For the method of spatial averages, we firstly obtained the spatial distribution of the temporal average within a  $1^\circ \times 1^\circ$  grid during the monsoon season. We then determined the spatial average based on the above temporal average in the entire South Asia. For the spatial patterns of temporal changes, we identified the results of the linear temporal changes in atmospheric conditions during monsoon season from 2006 to 2015. The surface solar radiation was analyzed in a relative sense with variable aerosols, clouds, and water vapor. Thus, this study mostly focuses on the relative changes in surface solar radiation but less on the calculated absolute values, which are importantly affected by different detection methods, sensitivities, and retrieval algorithms of sensors.

The cloud radiative effect (CRE) is widely used to quantify the degree of cloud–radiation interactions [24]. The present study is based on previous studies [28–30] in which the CRE in all-sky conditions is the net (down minus up) flux difference between the all- and clear-sky conditions at the atmosphere, surface, or TOA, as expressed in Equation (1):

$$CRE = \left( F^\downarrow - F^\uparrow \right)_{All-sky} - \left( F^\downarrow - F^\uparrow \right)_{Clear-sky} \quad (1)$$

where  $F^\downarrow$  and  $F^\uparrow$  are the downwelling and upwelling radiative fluxes at the TOA and surface, respectively. This study aims to quantify the effect of cloud variations at the TOA and surface fluxes. However, the CRE inferred from CERES is constantly disturbed by water vapor, aerosol, and the limited capability of combined MODIS to detect thin cirrus, mixed-phase clouds, and broken clouds [16]. Furthermore, CERES insufficiently considers the effect of multi-layer clouds [31]. Therefore, this study uses CloudSat 2B-FLXHR in evaluating the effects of cloud variations on radiation at the TOA and surface.

Moreover, this study uses precipitable water (PW) variation to describe the column changes of water vapor in the atmosphere. PW is the total water vapor in the atmospheric column, which is calculated based on the data on the environmental parameters from the ECMWF-AUX product, as defined in Equation (2):

$$PW = \frac{1}{g_0} \int_{P_{TOA}}^{P_{Surface}} q(P) dP \quad (2)$$

where  $g_0 = 9.8 \text{ m s}^{-2}$  is the standard acceleration caused by gravity at the mean sea level (m.s.l.),  $P$  is the atmospheric pressure, and  $q(P)$  is the specific humidity of air that exists as a function of the atmospheric pressure [32]. The PW data from the ECMWF-AUX are verified with a bias of approximately  $-1 \text{ mm}$  (depending on water vapor amount) compared with the observations from 21 Global Position System and 14 radiosonde stations [32]. Therefore, the PW data derived from the ECMWF-AUX can adequately indicate the changes in water vapor amount found in South Asia.

We accurately evaluated the effect of water vapor variations on solar radiation via BUGSrad. We used the environmental parameters, including temperature, pressure, specific humidity and cloud mask, provided by the CloudSat ECMWF-AUX products as the input for BUGSrad. Then, we varied only the average water vapor amount during the monsoon season, and other environmental parameters were fixed as the inter-annual average values to exclude the effect of other factors. We directly used the averaged environmental parameters for the radiative transfer model during the monsoon season to evaluate the radiative effect of water vapor by considering the quantity of the calculation. Because of the difference of averaged methods that were used by CloudSat and BUGSrad to evaluate the radiative effect of water vapor, several differences may show between the radiative fluxes calculated based on CloudSat and BUGSrad.

### 3. Results

#### 3.1. Changes in Aerosols

Figure 1a shows that aerosol loading increased and that the change in the average AOD detected by CALIPSO (approximately 0.13) was more intense than that detected by MODIS (approximately 0.05) during the monsoon season. Many factors are involved in contributing to the difference between MODIS and CALIPSO AOD, including cloud contamination, aerosol types, and vertical distribution. For example, the MODIS is more sensitive to cloud contamination compared with CALIPSO AOD, generally resulting in artificially high AOD retrieval by MODIS, due to the undetected thin clouds [33]. However, for biomass burning regions, CALIPSO AOD is significantly higher than MODIS AOD due to the strong absorption of smoke to solar radiation [34]. Moreover, the aerosol vertical distribution also importantly affects MODIS AOD retrieval, caused by the insufficient ability for MODIS to determine the vertical information of the aerosol layer [35]. Irrespective of the difference between MODIS and CALIPSO AOD, the CALIOP observations are consistent with the MODIS results for the geographical patterns and seasonal variations [36,37]. The change in the average AOD detected by CALIPSO exhibited a higher significance level ( $p = 0.07$ ) than that detected by MODIS ( $p = 0.22$ ). This result is has important contributions from the extensive cloud contamination on MODIS during the monsoon season [33].

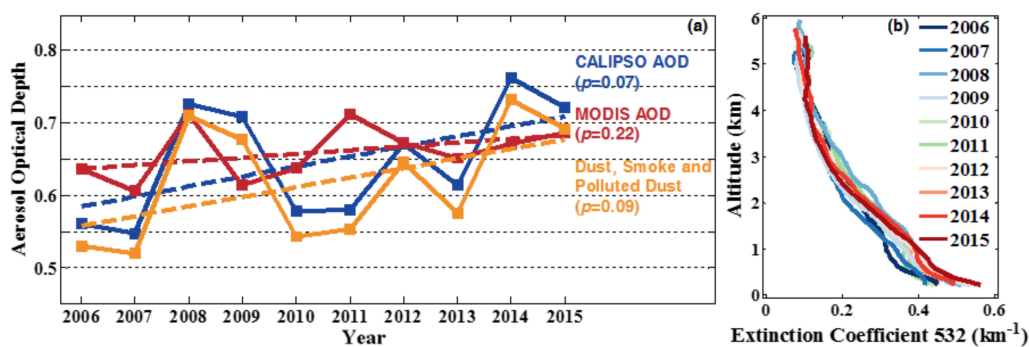


**Figure 1.** Temporal variations in spatial average AOD from (a) CALIPSO and MODIS during the monsoon season and (b) the vertical average aerosol extinction coefficient at 532 nm in South Asia from 2006 to 2015, respectively. The dashed lines indicate the linear fit line of the solid line with the same color;  $p$  is the significance level.

Additionally, the consistently robust and rapid increase in aerosols in South Asia have verified by satellite and ground-based observations from many previous studies [38–40]. Srivastava [39] found that the positive trends in AOD are found over the main continental regions of South Asia based on ground-based radiometric measurements. Kaskaoutis, et al. [40] exhibited overall increasing trends in AOD (7.69%) with a high significance based on Aerosol Robotic Network (AERONET) measurements

from 2001 to 2010 in northern India, which are consistent with satellite observations (MODIS) of increasing AOD and enhanced anthropogenic emissions over India. Moreover, Bibi, et al. [41] also reported a high degree of correlation (above 0.7) between the inter-comparison of MODIS AOD and AERONET data in India.

Figure 1b depicts the change in the vertically-averaged aerosol extinction coefficient at 532 nm during the study period. This profile is calculated by averaging all extinction coefficient values at the presence of aerosol in each point with a vertical interval of 240 m within the given spatial-temporal range, thereby indicating the total ability of aerosols to vertically scatter and absorb solar radiation. Moreover, to highlight the most probable altitude of the aerosol layer, we removed the points in which the occurrence frequency is one order of magnitude less than the maximum occurrence frequency of aerosol in vertical profiles. Figure 1b displays that the aerosol mostly occurs under 5 km m.s.l., and its extinction coefficient is exponentially weakened with the increase in altitude in South Asia. This result is consistent with previous work [42,43]. Moreover, the vertical aerosol extinction coefficient increases distinctly during the monsoon season in South Asia from 2006 to 2015, especially below 2 km.

Moreover, the sum of dust, smoke, and polluted dust aerosol loadings detected by CALIPSO is near the total loading of aerosol (orange and blue lines in Figure 1a). This result indicates that aerosols mostly consist of dust, smoke, and polluted dust during the monsoon season in South Asia, hence attaining consistency with previous work [44]. These aerosols present distinct absorbing effects on solar radiation, thereby attenuating the incoming solar radiation more intensively than other types of aerosols [45]. The incident SW radiation at the surface is highly negatively correlated with aerosol loading [15,46]. Aerosols can directly attenuate SSR by scattering and absorbing solar radiation (aerosol direct effect), or indirectly attenuate SSR via their capability to act as cloud condensation nuclei, thereby changing cloud reflectivity (aerosol indirect effects) [1]. Therefore, the increase in AOD negatively contributed to the recent brightening during the monsoon season in South Asia from 2006 to 2015.

### 3.2. Effects of Clouds

In this study, the cloud vertical frequency is defined as the ratio of the number of cloud bins to the total number of observed bins by CloudSat at different heights, referring to a previous study [47]. The cloud vertical frequency sequentially decreased during the monsoon season in South Asia from 2006 to 2015, with a maximum decrement of 7.1% (Figure 2a). In general, the cloud water content and number concentration of liquid and ice under cloudy conditions consistently decreased, with maximum decrements of  $18.0 \text{ mg m}^{-3}$  and  $1.4 \text{ mg m}^{-3}$  of liquid and ice water content (Figure 2b,e), and approximately  $6.0 \text{ cm}^{-3}$  and  $2.0 \text{ L}^{-3}$  of liquid and ice number concentration (Figure 2d,g), respectively. However, the liquid and ice effective radius variations were indistinct and inconsistent with the changes in cloud water content and number concentration. Therefore, the cloud vertical frequency decreased with the reduced cloud water content and number concentration, but no clear change was observed in the particle effective radius during the monsoon season in South Asia from 2006 to 2015.

In Figure 3a, the total cloud fraction detected by CloudSat declined by 8.8% ( $p = 0.07$ ) during the monsoon season in South Asia from 2006 to 2015. Furthermore, the change in cloud water path (CWP, which is the sum of the liquid and ice water paths) under cloudy conditions was consistent with that of the total cloud fraction with a decrement of  $34.7 \text{ g m}^{-2}$  ( $p < 0.01$ ). The uppermost cloud top height (CTH) declined by 661 m ( $p = 0.08$ ), and the cloud geometrical depth (CGD) declined by 280 m ( $p = 0.21$ ) with partial fluctuations in 2009 and 2010 (Figure 3b). By contrast, an insignificant trend occurred in the lowermost cloud base height (CBH) variation. Then, we further analyze the spatial variations in cloud fraction, cloud height (CH, which is the mean of corresponding CTH and CBH), CWP, and CGD. Figure 3c–f illustrate the consistent decreases in cloud fraction, CH, CWP, and CGD, especially for the cloud fraction and CWP with significant and consistent changes in space. The CH and CGD increased in certain parts of the western coastal area in South Asia. Overall, we can conclude that clouds decreased and thinned with the reduction in water content and particle

number concentration (Figure 2) during the monsoon season in South Asia from 2006 to 2015, thereby weakening the regulation of cloud on radiation.

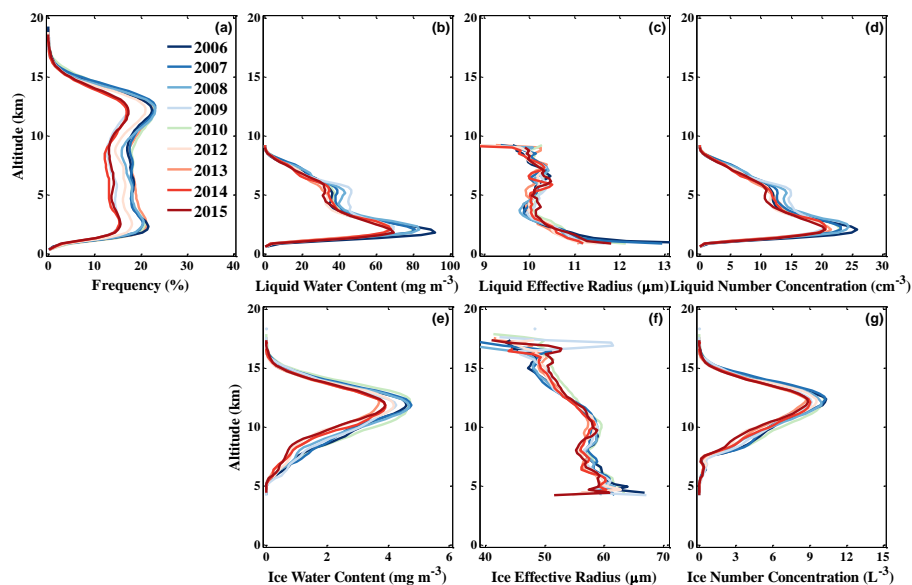


**Figure 2.** Temporal variations in spatial average vertical cloud physical parameters from CloudSat during the monsoon season in South Asia from 2006 to 2015: (a) cloud vertical frequency distribution, and liquid and ice (b,e) water content, (c,f) effective radius, and (d,g) number concentration.

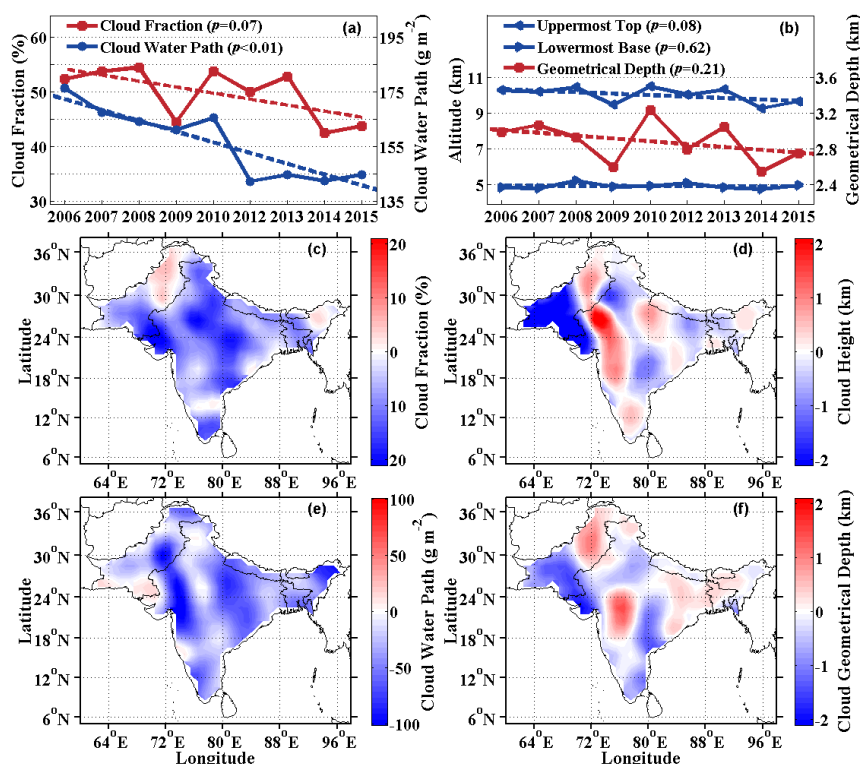


**Figure 3.** Temporal variations in spatial average (a) cloud fraction and CWP, as well as (b) uppermost CTH, lowermost CBH and CGD; spatial distributions of the temporal changes in average (c) cloud fraction, (d) CH, (e) CWP, and (f) CGD from CloudSat during the monsoon season in South Asia from 2006 to 2015. The dashed lines indicate the linear fit line of the solid line with the same color;  $p$  is the significance level.

The factors that contribute to the changes in clouds are complicated and varied in South Asia. Ackerman, et al. [48] verified that aerosols with intensive absorption may lead to evaporation in the cloud layers (the aerosol semi-direct effect), thereby burning off the clouds in South Asia, including widespread dust, polluted dust, and smoke. Bollasina, et al. [49] highlighted that anthropogenic aerosol emissions weaken the South Asian summer monsoon, thereby causing a decrease in the occurrence and amount of precipitation. Globally, observed and simulated cloud change patterns at the global scale are consistent with the poleward retreat of mid-latitude storm tracks. This result is attributed to the increase in greenhouse gas concentrations and recovery from volcanic radiative cooling [50]. In fact, the recent weakened rainfall and dried monsoon during the summer monsoon season were verified by many previous studies, given the reduction of clouds [49,51].

Consequently, we investigate the radiative force of cloud vertical variations to determine their possible contribution to the recent rapid brightening (Figure 4). We use the vertical heating rates in all-sky conditions to indicate the change in the vertically radiative effects of clouds. These effects are the results of cloud fraction, cloud vertical distribution, and cloud microphysical properties [26]. The SW heat rating decreased by around  $0.3\text{--}0.4\text{ K d}^{-1}$  at an altitude of  $5\text{--}15\text{ km}$  from 2006 to 2015, whereas a few increases in the SW heat rating occurred at low-level and near-surface areas (below  $3\text{ km}$ ). The total cloud reflection and absorption (mainly located at  $5\text{--}15\text{ km}$ ) weakened consistently with the reduction in clouds, thereby enhancing atmospheric transmission, causing further SW radiation to reach the near-surface area, and heating the low-level atmosphere and surface [24]. Because of the extremely minimal cloud detected by CloudSat at above  $15\text{ km}$ , no significant change in heat rating occurred above  $15\text{ km}$ , as demonstrated in the cloud vertical frequency distribution shown in Figure 2a.

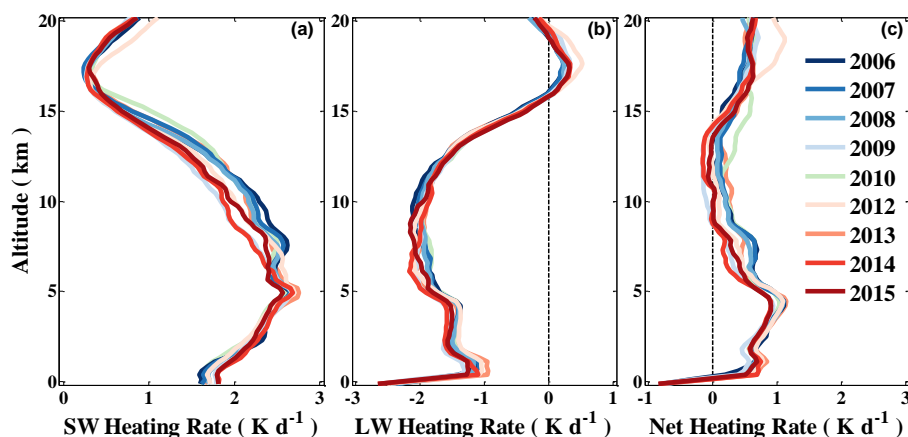


**Figure 4.** Temporal variations in spatial average vertical (a) SW, (b) LW, and (c) net heat rating in all-sky conditions from CloudSat during the monsoon season in South Asia from 2006 to 2015.

However, the change in LW vertical heating rate was indistinct compared with that of SW. Correspondingly, the LW radiative heating increased by less than  $0.2\text{ K d}^{-1}$  above  $10\text{ km}$ , whereas that of heating decreased by  $0.1\text{--}0.2\text{ K d}^{-1}$  within the cloud, especially below  $3\text{ km}$ , from 2006 to 2015. The total cloud LW absorption emitted from the surface decreased with the reduction in clouds, thereby leading to a weakened LW heating rate within the cloud layer (mainly below  $10\text{ km}$ ) and more LW emissions on the top cloud layer above  $10\text{ km}$  [18]. In general, the net vertical heating rate weakened consistently, thereby indicating that the changes in the physical characteristics of clouds result in the weakened vertical radiative effect of clouds.

When a cloud layer occurs, the incident solar radiation at the surface is generally reduced due to the absorption and reflection of cloud layers to solar radiation [24]. In Figure 5a, the SW CRE at the surface and TOA is weakened by approximately  $42.1$  and  $38.5\text{ W m}^{-2}$  with high significance levels  $p$  of  $0.05$  and  $0.04$ , respectively. This phenomenon indicates that the total absorption and reflection of cloud layers to solar radiation is weakened due to the cloud property variations, which thus leads to

consequentially enhancing the incident solar radiation at the surface. Although the CRE, derived from CloudSat, largely ignores the contribution of high thin clouds, this contribution is considerably smaller than that of low clouds [18,24]. Figure 5b presents the spatial distribution of the weakened SW CRE at the surface, which is the result of cloud property variations (Figure 3). The weakened SW CRE reaches its maximum and minimum in the central and northwest parts of South Asia, respectively. This spatial pattern of the weakened SW CRE is possibly attributed to complicated and diverse factors, including cloud spatial distribution (minimal cloud in the northwest part of South Asia), aerosol distribution (maximum in the central and northern part of South Asia), and terrain [38].

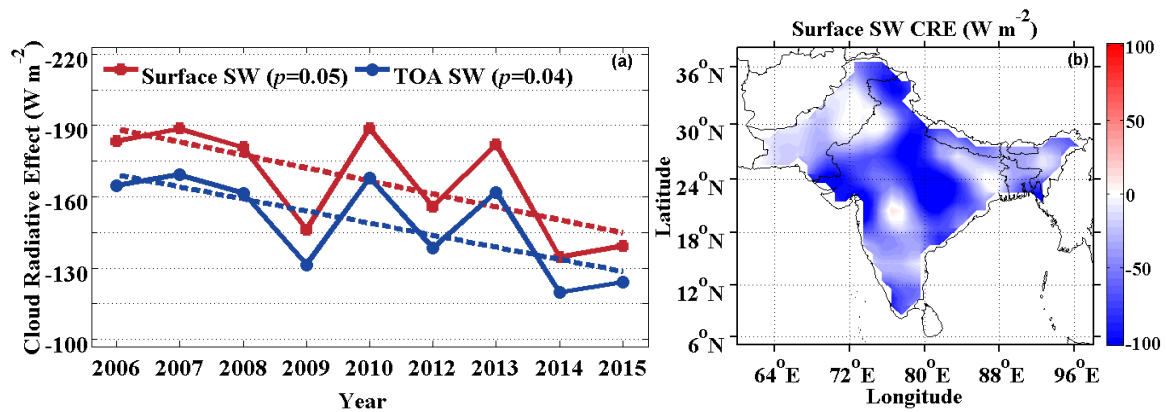


**Figure 5.** (a) Temporal variations in spatial average CRE at the TOA and surface, and (b) spatial distribution of the temporal changes in average SW CRE from CloudSat at the surface during the monsoon season in South Asia from 2006 to 2015. The dashed lines indicate the linear fit line of the solid line with the same color;  $p$  is the significance level.

### 3.3. Effects of Water Vapor

The water vapor importantly decreases the incident solar radiation at the surface due to its absorption of solar radiation [12]. Figure 6a,c exhibit the vertical relative humidity (RH) in all-sky and clear conditions, which consistently and gradually decreased with a maximum decrement of approximately 10% during the monsoon season in South Asia from 2006 to 2015. The spatial distributions of the temporal change of the PW are also highly consistent between all-sky and clear-sky conditions (Figure 6b,d). PW decreased in space with a maximum decrement of 6.6 mm in South Asia, especially in the western and central regions. Although a small increase in water vapor (less than 2 mm) occurred in the southern part of South Asia, the increment was considerably lower than the decrease in water vapor in most regions of South Asia. The decrease in atmospheric water vapor may be attributed to the weakened monsoon intensity in the recent decade during the monsoon season in South Asia [51].

Due to the intrinsically positive association of water vapor and clouds, we focus mainly on the effect of water vapor on solar radiation in clear-sky conditions to restrict the disturbance from clouds. Figure 7a depicts that radiation is highly and negatively correlated with PW from the ECMWF-AUX. Thus, water vapor is a substantial controlling factor in solar radiation variability. This control lies in the direct and indirect effects. The direct effect refers to the absorption of solar radiation in which the PW decreased by nearly 2.8 mm ( $p = 0.13$ ) over the brightening period. Based on the evaluation of BUGSrad, solar brightening was greater than  $2.5 W m^{-2}$  ( $p = 0.14$ ), given the weakened absorption caused by the decrease in water vapor. The SSR in clear-sky conditions from CloudSat increased by approximately  $4.8 W m^{-2}$  ( $p = 0.05$ ). Except for the contribution of water vapor variations, this radiative change was possibly caused by the change in atmospheric conditions and the incoming solar radiation provided by ECMWF-AUX and CloudSat [52].

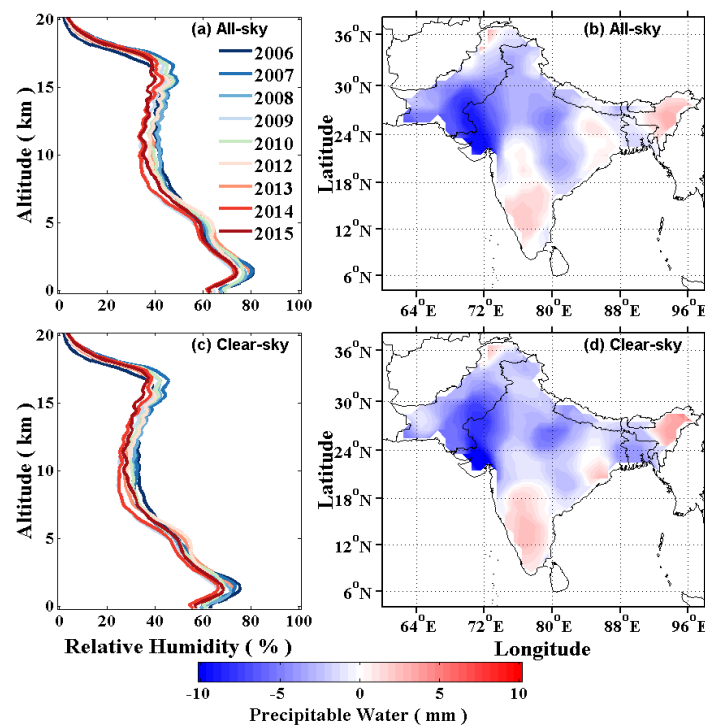


**Figure 6.** Temporal variations in spatial average vertical RH in (a) all-sky and (c) clear-sky conditions; spatial distribution of temporal changes in the average PW in (b) all-sky and (d) clear-sky conditions from the ECMWF-AUX during the monsoon season in South Asia from 2006 to 2015.

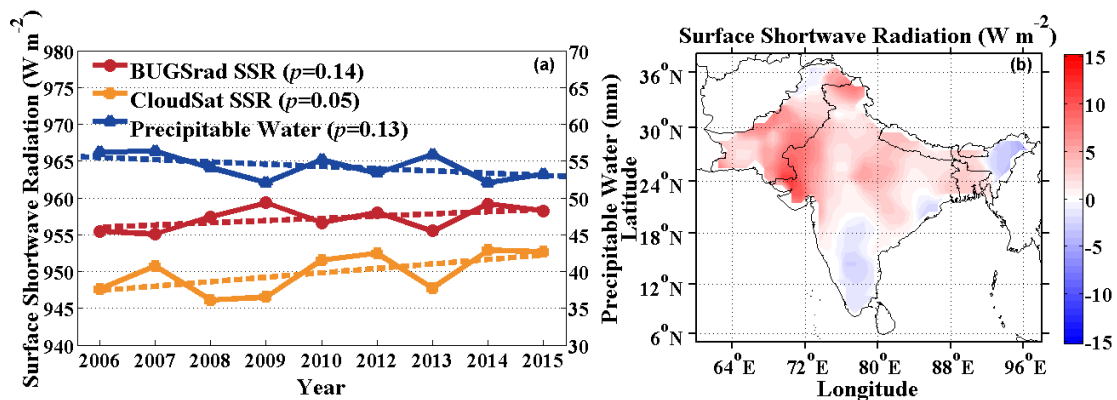


**Figure 7.** Temporal variations in spatial average (a) PW (blue line) and SSR in clear-sky conditions from BUGSrad (red line) and CloudSat (orange line); spatial distribution of temporal changes in average (b) SSR from BUGSrad in clear-sky conditions during the monsoon season in South Asia from 2006 to 2015. The dashed lines indicate the linear fit line of the solid line with the same color;  $p$  is the significance level.

The spatial variation in SSR in the clear-sky conditions was highly negative and consistent with that of PW (Figures 6d and 7b), especially in the western and central regions of South Asia, which partly consists of deserts. Furthermore, the indirect effects of water vapor occur in the all-sky conditions, and such effects are called water vapor–cloud interaction. Generally, a high concentration of water vapor favorably generates additional or robust convective clouds and results in decreased radiation at the surface, and vice versa [52]. Moreover, water vapor also regulates cloud amount by affecting the aerosol–cloud interaction, which generally shows a positive relationship under moist atmospheric conditions [53]. Therefore, the effect of water vapor is more complicated and uncertain in

the all-sky than in clear-sky conditions, considering the direct and indirect effects of water vapor on solar radiation.

To quantify the contribution of the variations of water vapor amount vertically, we calculate the PW at a different range of altitude (Figure 8). Water vapor mainly concentrates on the low-level altitude (<2 km) and rapidly decreases with altitude. The low-level PW decreased by 1.3 and 1.5 mm, with a high significance level in the all-sky ( $p = 0.04$ ) and clear-sky conditions ( $p = 0.05$ ). These changes dominated the total changes of water vapor amount during the monsoon season in South Asia from 2006 to 2015. Moreover, while the PW at a different range of altitude consistently decreased, the significance levels of trends gradually weakened with the increase in altitude, which indicates the large uncertainties in high-level water vapor variations. Overall, the water vapor importantly decreased during the monsoon season in South Asia from 2006 to 2015, which dominantly contributed by the low-level water vapor variations (below 2 km) with a high significance level. Consequentially, the decreased water vapor enhanced the incident solar radiation due to the reduction in atmospheric absorption from water vapor.

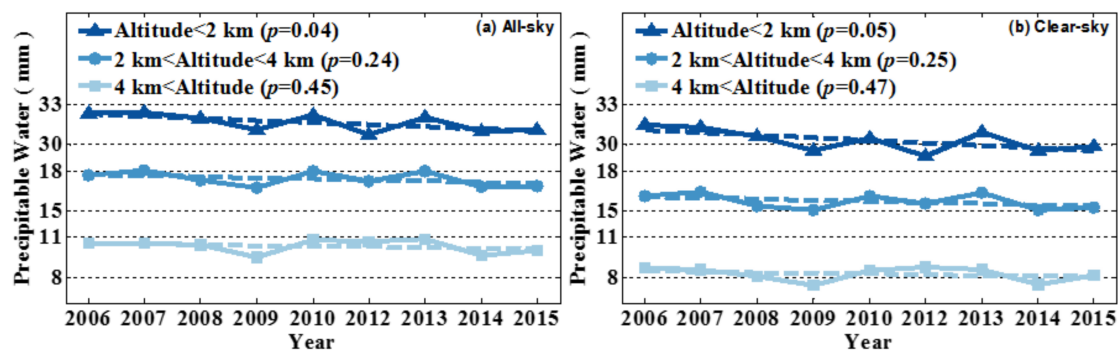


**Figure 8.** Temporal variations in spatial average PW in (a) all-sky and (b) clear-sky conditions at different ranges of altitude during the monsoon season in South Asia from 2006 to 2015. The dashed lines indicate the linear fit line of the solid line with the same color;  $p$  is the significance level.

#### 4. Extended Discussion of Seasonal Differences

Furthermore, we discuss the seasonal difference of aerosol, cloud, and water vapor variations and the correlated brightening/dimming in South Asia from 2006 to 2015. Figure 9 illustrates the recent changes in aerosol loading and SSR during the different seasons, namely, pre-monsoon, monsoon, and dry seasons, respectively, where the three seasons occur in March–May, June–September, and October–February, respectively. The AOD consistently increased around the entire year (Figure 9a), whereas the increments of the AOD were greater during the pre-monsoon and dry seasons, by 0.08 and 0.11, respectively, than during the monsoon season from 2006 to 2015. The significance level of the AOD variation detected by MODIS was higher during the non-monsoon season ( $p < 0.01$ ) than during the monsoon season ( $p < 0.22$ ), primarily because of the disturbance of widespread clouds during the monsoon season [16]. The AOD detected by MODIS is inevitably affected by cloud contaminations caused by thin and mixed-phase clouds undetected by MODIS, broken cloud layers, and precipitating clouds [53,54]. Moreover, the accuracy and significance of MODIS observations are considerably lower during monsoon season with widespread clouds than during the pre-monsoon and dry seasons with insufficient clouds in South Asia [55].

With the resultant change of aerosol, cloud, water vapor, and others factors, the average SSR (red line) in the all-sky conditions from CERES increased by  $16.2 \text{ W m}^{-2}$  increments during the monsoon season in South Asia from 2006 to 2015. These phenomena indicate that the attenuating effect of the atmosphere on solar radiation gradually weakened, thereby increasing the incident solar radiation at the surface (brightening). Moreover, the significance level of 0.40 during the monsoon season also indicates the instability in the recent transition from dimming to brightening [9]. However,

Figure 9b displays no distinct change in the SSR during the pre-monsoon season, while even the significant reverse trend of SSR during the dry season (dimming) compared with that of during the monsoon season.

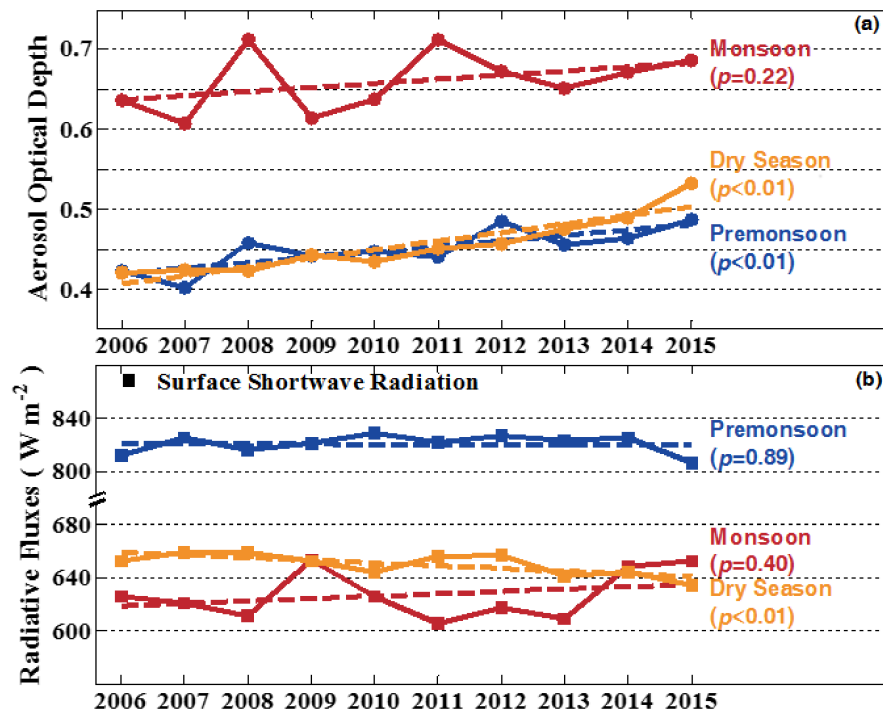


**Figure 9.** Temporal variations in (a) spatial average AOD from MODIS and (b) SSR from CERES during the pre-monsoon, monsoon, and dry seasons in South Asia from 2006 to 2015, respectively. The dashed lines indicate the linear fit line of the solid line with the same color;  $p$  is the significance level.

Many reasons can contribute to the seasonal difference of SSR variations. Aerosols dominate the change in the solar radiation that reaches the surface in clear-sky conditions [9]. Therefore, aerosols exhibit a greater weight effect on solar radiation during the dry season than during the monsoon season. The increase in aerosol loading directly contributes to the decrease in the SSR, thereby resulting in the dimming during the dry season with low cloud cover, which is consistent with the study of Folini and Wild [15]. In addition, the resultant of the impacts of 3D aerosol, cloud, and water vapor are considerably complicated and varied given the intensive atmospheric activities during the monsoon season, and hence, this observation possibly contributes to the fluctuation of SSR variations during the monsoon season. The pre-monsoon season is the transition period from the dry to the monsoon seasons and is associated with establishing the southwestern wind regime over South Asia [44]. The atmospheric condition and radiation variations are indistinct compared with the trend of the SSR between the dry and monsoon seasons.

## 5. Conclusions

We use observations from multiple satellites/sensors in the A-Train satellite constellation to evaluate the impacts of 3D aerosol, cloud, and water vapor variations on the recent changes in solar radiation on the Earth's surface during the monsoon season (June–September) in South Asia from 2006 to 2015. The satellites used mainly include CloudSat, CALIPSO, MODIS, and CERES. We illustrate the results of this study in Figure 10 and summarize these results as follows.

We found that the SSR possibly increased by  $16.2 \text{ W m}^{-2}$  with a partial fluctuation based on the CERES observation during the monsoon season. By contrast, the increase in aerosol loading (mainly below 2 km) was inconsistent with the SSR variation and did not contribute to the recent brightening in

South Asia. Decreases in water vapor amount and clouds significantly contributed to solar brightening and, possibly, subsequent surface warming in South Asia. In general, the clouds are reduced and thinned by approximately 8.8% and 280 m, respectively, when the CWP (by  $34.7 \text{ g m}^{-2}$ ) and particle number concentration under cloudy conditions decreased. Correspondingly, the SW CRE weakened by approximately  $42.1 \text{ W m}^{-2}$  at the surface. Moreover, the PW in clear-sky conditions possibly decreased by nearly 2.8 mm over the brightening period. The decreased PW is dominated by low-level water vapor (below 2 km), which decreased by 1.5 mm in clear-sky conditions with a high significance level. Consequently, solar brightening increased by approximately  $2.5 \text{ W m}^{-2}$  because of the weakened absorption of water vapor in clear-sky conditions. The decreases in 3D water vapor amount and clouds weakened the effect of water vapor and clouds on solar radiation, thereby resulting in the increased absorption of direct solar radiation at the surface and subsequent surface brightening.

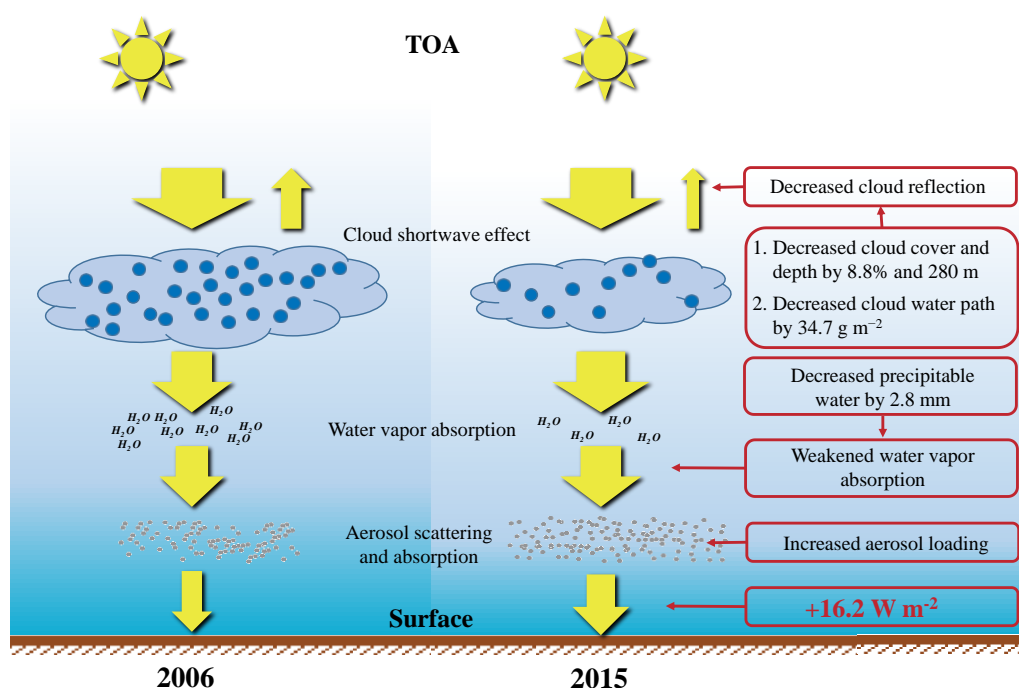


**Figure 10.** Schematic of the impacts of 3D aerosol, cloud, and water vapor variations on brightening during the monsoon season in South Asia from 2006 to 2015. Background gradient color represents the changing RH. The relative humidity is high when the color is dark.

The conclusions of this study are beneficial in evaluating the recent variations in 3D aerosol, cloud, and water vapor and their resultant impacts on solar radiation. Notably, the data in this study were from the instantaneous observations of multiple sensors. We then use the observations to ensure consistently observed conditions of multiple satellites from the A-Train. Thus, the magnitudes of radiative impact may be overestimated for the water vapor and cloud variations. The results are more representative of the atmospheric condition variations at nominally constant solar zenith angles than the daily average. Additionally, solar dimming and brightening may be of a local or regional nature [9]. The variations in aerosols, water vapor, and clouds highly interact with changes in monsoon circulation in South Asia. Thus, investigating the change mechanisms of aerosols, clouds, and water vapor in South Asia is interesting. The chicken-and-egg relationship between monsoon and aerosols, and water vapor and clouds can also be explored.

**Supplementary Materials:** The following are available online at <http://www.mdpi.com/2072-4292/10/4/651/s1>, Table S1: Observations used in the analysis along with their sources and spatial resolutions, Figure S1: Terrain map during the monsoon season in South Asia and the surrounding regions. The blue line indicates rivers; the study region is within the red line.

**Acknowledgments:** This study is supported by the National Key R&D Program of China (2017YFC0212600, 2016YFC0200900) and the National Natural Science Foundation of China (41701381, 41627804). We are grateful to the science teams for providing excellent and accessible data of the CloudSat (cloudsat.cira.colostate.edu), CALIPSO and CERES (eosweb.larc.nasa.gov), and MODIS (ladsweb.modaps.eosdis.nasa.gov).

**Author Contributions:** Z.P. and F.M. conceived and designed the research. Z.P., and W.W. conducted the analysis and performed manuscript writing. X.L. and B.Z. refined the interpretations. W.G. and F.M. discussed the results and implications, provided comments and contributed to the text.

**Conflicts of Interest:** The authors declare no conflict of interest.

## Abbreviations

The following abbreviations are used in this manuscript:

3D	Three-dimensional
AERONET	Aerosol Robotic Network
AOD	Aerosol optical depth
CALIPSO	Cloud–Aerosol Lidar and Infrared Pathfinder Satellite Observations
CBH	Cloud base height
CERES	Clouds and the Earth’s Radiant Energy System
CGD	Cloud geometrical depth
CH	Cloud height
CRE	Cloud radiative effect
CTH	Cloud top height
CWP	Cloud water path
ECMWF	European Centre for Medium-Range Weather Forecast
MODIS	Moderate Resolution Imaging Spectroradiometer
PW	Precipitable water
RH	Relative humidity
SW	Shortwave
LW	Longwave
SSR	Surface shortwave radiation
TOA	Top of atmosphere

## References

1. Wild, M. Enlightening Global Dimming and Brightening. *Bull. Am. Meteorol. Soc.* **2012**, *93*, 27–37. [[CrossRef](#)]
2. Wild, M.; Gilgen, H.; Roesch, A.; Ohmura, A.; Long, C.N.; Dutton, E.G.; Forgan, B.; Kallis, A.; Russak, V.; Tsvetkov, A. From dimming to brightening: Decadal changes in solar radiation at Earth’s surface. *Science* **2005**, *308*, 847–850. [[CrossRef](#)] [[PubMed](#)]
3. Haywood, J.M.; Nicolas, B.; Andy, J.; Olivier, B.; Martin, W.; Shine, K.P. The roles of aerosol, water vapor and cloud in future global dimming/brightening. *J. Geophys. Res. Atmos.* **2011**, *116*, D20. [[CrossRef](#)]
4. Liepert, B.G. Observed reductions of surface solar radiation at sites in the United States and worldwide from 1961 to 1990. *Geophys. Res. Lett.* **2002**, *29*, 61-1–61-4. [[CrossRef](#)]
5. Long, C.N.; Dutton, E.G.; Augustine, J.A.; Wiscombe, W.; Wild, M.; Mcfarlane, S.A.; Flynn, C.J. Significant decadal brightening of downwelling shortwave in the continental United States. *J. Geophys. Res. Atmos.* **2009**, *114*, 1291–1298. [[CrossRef](#)]
6. Wild, M. Global dimming and brightening: A review. *J. Geophys. Res. Atmos.* **2009**, *114*, D00D16. [[CrossRef](#)]
7. Wild, M.; Trüssel, B.; Ohmura, A.; Long, C.N.; König-Langlo, G.; Dutton, E.G.; Anatoly, T. Global dimming and brightening: An update beyond 2000. *J. Geophys. Res. Atmos.* **2009**, *114*, 895–896. [[CrossRef](#)]
8. Wang, Y.; Wild, M. A new look at solar dimming and brightening in China. *Geophys. Res. Lett.* **2016**, *43*, 11777–11785. [[CrossRef](#)]
9. Soni, V.K.; Pandithurai, G.; Pai, D.S. Is there a transition of solar radiation from dimming to brightening over India? *Atmos. Res.* **2016**, *169*, 209–224. [[CrossRef](#)]
10. Padma, K.B.; Londhe, A.L.; Daniel, S.; Jadhav, D.B. Observational evidence of solar dimming: Offsetting surface warming over India. *Geophys. Res. Lett.* **2007**, *34*, 377–390.

11. Willson, R.C.; Mordvinov, A.V. Secular total solar irradiance trend during solar cycles 21–23. *Geophys. Res. Lett.* **2003**, *30*, 1199. [[CrossRef](#)]
12. Kim, D.; Ramanathan, V. Solar radiation budget and radiative forcing due to aerosols and clouds. *J. Geophys. Res. Atmos.* **2008**, *113*, 194–204. [[CrossRef](#)]
13. Kvalevåg, M.M.; Myhre, G. Human Impact on Direct and Diffuse Solar Radiation during the Industrial Era. *J. Clim.* **2007**, *20*, 4874–4883. [[CrossRef](#)]
14. Kambezidis, H.D.; Kaskaoutis, D.G.; Kharol, S.K.; Moorthy, K.K.; Satheesh, S.K.; Kalapureddy, M.C.R.; Badarinath, K.V.S.; Sharma, A.R.; Wild, M. Multi-decadal variation of the net downward shortwave radiation over south Asia: The solar dimming effect. *Atmos. Environ.* **2012**, *50*, 360–372. [[CrossRef](#)]
15. Folini, D.; Wild, M. Aerosol emissions and dimming/brightening in Europe: Sensitivity studies with ECHAM5-HAM. *J. Geophys. Res. Atmos.* **2011**, *116*, 21104. [[CrossRef](#)]
16. Remer, L.A.; Kaufman, Y.J.; Tanré, D.; Mattoo, S.; Chu, D.A.; Martins, J.V.; Li, R.R.; Ichoku, C.; Levy, R.C.; Kleidman, R.G. The MODIS Aerosol Algorithm, Products, and Validation. *J. Atmos. Sci.* **2005**, *62*, 947–973. [[CrossRef](#)]
17. Winker, D.M.; Pelon, J.; Coakley, J.A.; Ackerman, S.A.; Charlson, R.J.; Colarco, P.R.; Flamant, P.; Fu, Q.; Hoff, R.M.; Kittaka, C. The CALIPSO Mission: A Global 3D View of Aerosols and Clouds. *Bull. Am. Meteorol. Soc.* **2010**, *91*, 1211–1229. [[CrossRef](#)]
18. L'Ecuyer, T.S.; Wood, N.B.; Haladay, T.; Stephens, G.L.; Stackhouse, P.W. Impact of clouds on atmospheric heating based on the R04 CloudSat fluxes and heating rates data set. *J. Geophys. Res. Atmos.* **2008**, *113*, 2013–2018. [[CrossRef](#)]
19. Uppala, S.M.; Kållberg, P.W.; Simmons, A.J.; Andrae, U.; Bechtold, V.D.C.; Fiorino, M.; Gibson, J.K.; Haseler, J.; Hernandez, A.; Kelly, G.A. The ERA-40 re-analysis. *Q. J. R. Meteorol. Soc.* **2005**, *131*, 2961–3012. [[CrossRef](#)]
20. Loeb, N.G.; Wielicki, B.A.; Doelling, D.R.; Kato, S.; Wong, T.; Smith, G.L.; Keyes, D.F.; Manalosph, N. Toward optimal closure of the earth's top-of-atmosphere radiation budget. *J. Clim.* **2009**, *22*, 748–766. [[CrossRef](#)]
21. Omar, A.H.; Winker, D.M.; Kittaka, C.; Vaughan, M.A.; Liu, Z.; Hu, Y.; Trepte, C.R.; Rogers, R.R.; Ferrare, R.A.; Lee, K.-P. The CALIPSO Automated Aerosol Classification and Lidar Ratio Selection Algorithm. *J. Atmos. Ocean. Technol.* **2009**, *26*, 1994. [[CrossRef](#)]
22. Hu, Y.; Winker, D.; Vaughan, M.; Lin, B.; Omar, A.; Trepte, C.; Flittner, D.; Yang, P.; Nasiri, S.L.; Baum, B. CALIPSO/CALIOP Cloud Phase Discrimination Algorithm. *J. Atmos. Ocean. Technol.* **2009**, *26*, 2293–2309. [[CrossRef](#)]
23. Pan, Z.; Gong, W.; Mao, F.; Li, J.; Wang, W.; Li, C.; Min, Q. Macrophysical and optical properties of clouds over East Asia measured by CALIPSO. *J. Geophys. Res. Atmos.* **2015**, *120*, 11653–11668. [[CrossRef](#)]
24. Henderson, D.S.; L'Ecuyer, T.; Stephens, G.; Partain, P.; Sekiguchi, M. A Multisensor Perspective on the Radiative Impacts of Clouds and Aerosols. *J. Appl. Meteorol. Climatol.* **2013**, *52*, 853–871. [[CrossRef](#)]
25. Mace, G.G.; Zhang, Q. The CloudSat radar-lidar geometrical profile product (RL-GeoProf): Updates, improvements, and selected results. *J. Geophys. Res. Atmos.* **2014**, *119*, 9441–9462. [[CrossRef](#)]
26. Fu, Q.; Liou, K.N. On the Correlated k-Distribution Method for Radiative Transfer in Nonhomogeneous Atmospheres. *J. Atmos. Sci.* **1992**, *49*, 2139–2156. [[CrossRef](#)]
27. Stephens, G.L.; Gabriel, P.M.; Partain, P.T. Parameterization of Atmospheric Radiative Transfer. Part I: Validity of Simple Models. *J. Atmos. Sci.* **2001**, *58*, 3391–3409. [[CrossRef](#)]
28. Pan, Z.; Mao, F.; Gong, W.; Min, Q.; Wang, W. The warming of Tibetan Plateau enhanced by 3D variation of low-level clouds during daytime. *Remote Sens. Environ.* **2017**, *198*, 363–368. [[CrossRef](#)]
29. Logan, T.; Xi, B.; Dong, X. Aerosol properties and their influences on marine boundary layer cloud condensation nuclei at the ARM mobile facility over the Azores. *J. Geophys. Res. Atmos.* **2014**, *119*, 4859–4872. [[CrossRef](#)]
30. Li, S.; Joseph, E.; Min, Q.; Yin, B. Multi-year ground-based observations of aerosol-cloud interactions in the Mid-Atlantic of the United States. *J. Quant. Spectrosc. Radiat. Transf.* **2016**, *188*, 192–199. [[CrossRef](#)]
31. Sohn, B.J.; Nakajima, T.; Satoh, M.; Jang, H.S. Impact of different definitions of clear-sky flux on the determination of longwave cloud radiative forcing: NICAM simulation results. *Atmos. Chem. Phys.* **2010**, *10*, 11641–11646. [[CrossRef](#)]

32. Bock, O.; Keil, C.; Richard, E.; Flamant, C.; Bouin, M.N. Validation of precipitable water from ECMWF model analyses with GPS and radiosonde data during the MAP SOP. *Q. J. R. Meteorol. Soc.* **2010**, *131*, 3013–3036. [[CrossRef](#)]
33. Grandey, B.S.; Stier, P.; Wagner, T.M. Investigating relationships between aerosol optical depth and cloud fraction using satellite, aerosol reanalysis and general circulation model data. *Atmos. Chem. Phys.* **2013**, *17*, 30805–30823. [[CrossRef](#)]
34. Ma, X.; Bartlett, K.; Harmon, K.; Yu, F. Comparison of AOD between CALIPSO and MODIS: Significant differences over major dust and biomass burning regions. *Atmos. Meas. Tech.* **2013**, *6*, 2391–2401. [[CrossRef](#)]
35. Tian, P.; Cao, X.; Zhang, L.; Sun, N.; Sun, L.; Logan, T.; Shi, J.; Wang, Y.; Ji, Y.; Lin, Y. Aerosol vertical distribution and optical properties over China from long-term satellite and ground-based remote sensing. *Atmos. Chem. Phys.* **2017**, *17*, 1–47. [[CrossRef](#)]
36. Yu, H.; Chin, M.; Winker, D.M.; Omar, A.H.; Liu, Z.; Kittaka, C.; Diehl, T. Global view of aerosol vertical distributions from CALIPSO lidar measurements and GOCART simulations: Regional and seasonal variations. *J. Geophys. Res. Atmos.* **2010**, *115*, D4. [[CrossRef](#)]
37. Guo, J.; Liu, H.; Wang, F.; Huang, J.; Xia, F.; Lou, M.; Wu, Y.; Jiang, J.H.; Xie, T.; Zhaxi, Y. Three-dimensional structure of aerosol in China: A perspective from multi-satellite observations. *Atmos. Res.* **2016**, *178–179*, 580–589. [[CrossRef](#)]
38. Suresh, B.S.; Manoj, M.R.; Krishna, M.K.; Gogoi, M.M.; Nair, V.S.; Kumar, K.S.; Satheesh, S.K.; Niranjan, K.; Ramagopal, K.; Bhuyan, P.K. Trends in aerosol optical depth over Indian region: Potential causes and impact indicators. *J. Geophys. Res. Atmos.* **2013**, *118*, 11, 794–711, 806.
39. Srivastava, R. Trends in aerosol optical properties over South Asia. *Int. J. Clim.* **2016**, *37*, 371–380. [[CrossRef](#)]
40. Kaskaoutis, D.G.; Singh, R.P.; Gautam, R.; Sharma, M.; Kosmopoulos, P.G.; Tripathi, S.N. Variability and trends of aerosol properties over Kanpur, northern India using AERONET data (2001–10). *Environ. Res. Lett.* **2012**, *7*, 24003–24009. [[CrossRef](#)]
41. Bibi, H.; Alam, K.; Chishtie, F.; Bibi, S.; Shahid, I.; Blaschke, T. Intercomparison of MODIS, MISR, OMI, and CALIPSO aerosol optical depth retrievals for four locations on the Indo-Gangetic plains and validation against AERONET data. *Atmos. Environ.* **2015**, *111*, 113–126. [[CrossRef](#)]
42. Thorsen, T.J.; Fu, Q. CALIPSO-inferred aerosol direct radiative effects: Bias estimates using ground-based Raman lidars. *J. Geophys. Res. Atmos.* **2016**, *120*, 12–209. [[CrossRef](#)]
43. Li, S.; Joseph, E.; Min, Q. Remote sensing of ground-level PM<sub>2.5</sub> combining AOD and backscattering profile. *Remote Sens. Environ.* **2016**, *183*, 120–128. [[CrossRef](#)]
44. Das, S.; Dey, S.; Dash, S.K.; Giuliani, G.; Solmon, F. Dust aerosol feedback on the Indian summer monsoon: Sensitivity to absorption property. *J. Geophys. Res. Atmos.* **2015**, *120*, 9642–9652. [[CrossRef](#)]
45. Logan, T.; Xi, B.; Dong, X.; Li, Z.; Cribb, M. Classification and investigation of Asian aerosol absorptive properties. *Atmos. Chem. Phys.* **2013**, *13*, 2253–2265. [[CrossRef](#)]
46. Ruiz-Arias, J.A.; Gueymard, C.A.; Santos-Alamillos, F.J.; Pozo-Vázquez, D. Worldwide impact of aerosol's time scale on the predicted long-term concentrating solar power potential. *Sci. Rep.* **2016**, *6*, 30546. [[CrossRef](#)] [[PubMed](#)]
47. Luo, Y.; Zhang, R.; Wang, H. Comparing occurrences and vertical structures of hydrometeors between eastern China and the Indian monsoon region using CloudSat/CALIPSO data. *J. Clim.* **2009**, *22*, 1052–1064. [[CrossRef](#)]
48. Ackerman, A.S.; Toon, O.B.; Stevens, D.E.; Heymsfield, A.J.; Ramanathan, V.; Welton, E.J. Reduction of tropical cloudiness by soot. *Science* **2000**, *288*, 1042–1047. [[CrossRef](#)] [[PubMed](#)]
49. Bollasina, M.A.; Ming, Y.; Ramaswamy, V. Anthropogenic Aerosols and the Weakening of the South Asian Summer Monsoon. *Science* **2011**, *334*, 502–505. [[CrossRef](#)] [[PubMed](#)]
50. Norris, J.R.; Allen, R.J.; Evan, A.T.; Zelinka, M.D.; O'Dell, C.W.; Klein, S.A. Evidence for climate change in the satellite cloud record. *Nature* **2016**, *536*, 72. [[CrossRef](#)] [[PubMed](#)]
51. Turner, A.G.; Annamalai, H. Climate change and the South Asian summer monsoon. *Nat. Clim. Chang.* **2012**, *2*, 587–595. [[CrossRef](#)]
52. Yang, K.; Ding, B.; Qin, J.; Tang, W.; Ning, L.; Lin, C. Can aerosol loading explain the solar dimming over the Tibetan Plateau. *Geophys. Res. Lett.* **2012**, *39*, L20710. [[CrossRef](#)]
53. Christensen, M.W.; Chen, Y.C.; Stephens, G.L. Aerosol indirect effect dictated by liquid clouds. *J. Geophys. Res. Atmos.* **2016**, *121*, 14636–14650. [[CrossRef](#)]

54. Wang, W.; Mao, F.; Pan, Z.; Du, L.; Gong, W. Validation of VIIRS AOD through a Comparison with a Sun Photometer and MODIS AODs over Wuhan. *Remote Sens.* **2017**, *9*, 403. [[CrossRef](#)]
55. Levy, R.C.; Mattoo, S.; Munchak, L.A.; Remer, L.A. The Collection 6 MODIS aerosol products over land and ocean. *Atmos. Meas. Tech.* **2013**, *6*, 2989–3034. [[CrossRef](#)]



© 2018 by the authors. Licensee MDPI, Basel, Switzerland. This article is an open access article distributed under the terms and conditions of the Creative Commons Attribution (CC BY) license (<http://creativecommons.org/licenses/by/4.0/>).